Catalysis Letters (2020) 150:1061–1071
https://doi.org/10.1007/s10562-019-02991-5

Enhanced Photocatalytic Reduction of CO_2 on Rutile TiO_2/MgAl Layered Double Oxides with H_2O Under Ambient Temperature

Ruifeng Chong[1] · Caihong Su[1] · Zhenzhen Wang[1] · Zhixian Chang[1] · Ling Zhang[1] · Deliang Li[1]

Received: 2 August 2019 / Accepted: 30 September 2019 / Published online: 15 October 2019

Abstract

Photocatalytic reduction of CO_2 with H_2O is a fascinating approach to convert CO_2 into available fuels using solar energy as driven force. However, it still suffers from low efficiency owing to the instinct stability of CO_2. In this work, a hybrid photocatalyst of rutile TiO_2 nanorods supported on MgAl layered double oxides (TiO_2/MgAl-LDO) were designed and facilely fabricated via an in situ growth followed by a high temperature calcination process. The resulted TiO_2/MgAl-LDO demonstrated significantly enhanced photocatalytic reduction of CO_2 with the optimal CO and CH_4 evolution of 0.65 and 1.60 μmol in 8 h reaction under ambient temperature, which is ca. 4.6 and 48 times that of TiO_2 respectively. X-ray photoelectron spectroscopy revealed a strong electron interaction between TiO_2 and MgAl-LDO, as well as electrochemical characterization showed enhanced photocurrent, suggesting a promoted charge separation in photocatalytic process. CO_2-temperature-programmed desorption (CO_2-TPD) unveiled the relatively active bicarbonate, bidentate carbonate and monodentate carbonate species were formed on MgAl-LDO, which could boost the CO_2 reduction half-reaction. Meanwhile, NH_3-TPD revealed acidic sites existed in TiO_2/MgAl-LDO, which could act as active sites for H_2O adsorption and activation and thus promote the H_2O oxidation half-reaction. The strategy of simultaneous promotion on the reduction and the oxidation half-reactions will open a new vane to fabricate highly efficient catalysts toward photocatalytic reduction of CO_2 with H_2O.

Graphical Abstract

A hybrid photocatalyst of MgAl layered double oxides supported rutile TiO_2 with abundant acidic and/or basic sites exhibit significant enhancement on the photocatalytic reduction of CO_2 with H_2O under ambient temperature.

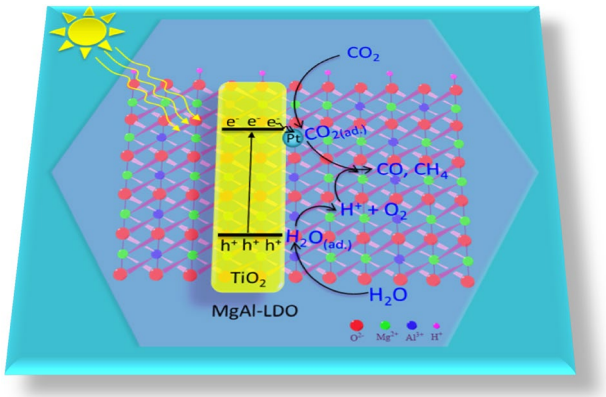

Keywords Photocatalysis · CO_2 reduction · MgAl layered double oxides · Rutile TiO_2

Electronic supplementary material The online version of this article (https://doi.org/10.1007/s10562-019-02991-5) contains supplementary material, which is available to authorized users.

Extended author information available on the last page of the article

1 Introduction

The photocatalytic reduction of CO_2 with H_2O to hydrocarbon over light excited semiconductors, which was inspired from natural photosynthesis, offers a fascinating strategy to reduce CO_2 emission and solve energy crisis [1–5]. Since the pioneering discovery of photocatalytic conversion of CO_2 into CH_3OH, CH_4, HCHO and HCOOH over semiconductors such as SiC, GaP and TiO_2 suspension by Inoue et al. [6], various efficient and ecofriendly semiconductor-based photocatalysts (including TiO_2 [7, 8], C_3N_4 [9–11] and ZnO [12], etc.) have been developed to realize photocatalytic reduction of CO_2 with H_2O. Among these photocatalysts, TiO_2 has received great attractions due to it high physicochemical stability, elemental abundance, ease availability and nontoxicity [7]. However, the photocatalytic reduction of CO_2 over TiO_2 still suffers from low efficiency. To improve the photocatalytic performance, many efforts have been devoted to optimizing the separation of photogenerated electrons and holes pairs, such as the construction of facet-based homojunctions [13] and crystalline phase-based homojunctions [14], or the decoration with noble metals (e.g., Pt) [15], transition metal (e.g., Cu) [16] and alloy (e.g. PtRu) [17]. In spite of these progresses, apparent quantum efficiencies (AQE) for photocatalytic reduction of CO_2 with H_2O over TiO_2 remains lower than 1% and the reaction rates are typically in the range of $\mu mol \cdot g^{-1} \cdot h^{-1}$ [18], which is severely insufficient for any practical applications.

In fact, as CO_2 is an extremely stable molecule with a higher dissociation energy of C=O bond (~ 750 kJ mol^{-1}), the low adsorption and the poor activation of CO_2 over the surface of photocatalyst are the biggest challenge for photocatalytic reduction of CO_2. Literature reported the first step in photocatalytic CO_2 reduction was the transformation from CO_2 to $CO_2^{\cdot -}$ by a single electron transfer from the catalyst. However, such transformation required to overcome an energy barrier as high as − 1.90 V versus NHE [19, 20]. The surface chemistry of CO_2 on oxides verified the energy barrier could be significantly decreased by enhancing the interaction between CO_2 and oxides surface, which induced various adsorption model of CO_2 on oxides surface [21, 22]. Inspired by such consideration, CO_2 adsorbents, such as NaOH [23] and MgO [24–28], have been widely employed as promoters to construct TiO_2-based photocatalysts, due to their superior adsorption capacity for CO_2. For example, NaOH could enhance the chemisorption of CO_2 by forming carbonate and/or $CO_2^{\cdot -}$, while MgO was beneficial for CO_2 adsorption to form carbonate. As results, TiO_2 modified with NaOH and MgO exhibited enhanced performance for the photocatalytic reduction of CO_2, which was mainly attributed to the accelerated CO_2 reduction half-reaction. However, owing to the strong basic character, these compounds inevitably suffered from the carbonation and subsequent deactivation, resulting in instability of the photocatalysts. On the other hand, the photocatalytic reduction of CO_2 with H_2O was also inevitably accompanied with the H_2O oxidation half-reaction, which was an energetically uphill reaction involved a four-electron transfer process. The lower oxidation of H_2O would lead to the accumulation of charges and cause recombination of separated charges. Thus, the oxidation of H_2O was also a challenge during the photocatalytic CO_2 reduction.

In view of the above considerations, both CO_2 reduction and H_2O oxidation half-reactions are important in the process of photocatalytic reduction of CO_2 with H_2O. The modifiers, which could not only facilitate the CO_2 reduction half-reaction but also promote the H_2O oxidation half-reaction, would significantly enhance the photocatalytic reduction of CO_2 with H_2O [29]. MgAl layered double oxides (MgAl-LDOs), which derived from MgAl layered double hydroxides (MgAl-LDHs), have recently been found with great potential to enhance the photocatalytic reduction of CO_2 with H_2O on TiO_2 nanorods [30], where MgAl-LDO exhibited excellent performance that enhanced the adsorption/activation of CO_2 and the adsorption/dissociation of H_2O (namely, the half-reactions of CO_2 reduction and water oxidation). However, the efficiency for the photocatalytic reduction of CO_2 remains low and requires further investigations to achieve highly efficient photocatalysts based on TiO_2 and MgAl-LDO. Therefore, in the present work, rutile TiO_2 nanorods were supported on MgAl-LDO substrate to fabricated TiO_2/MgAl-LDO hybrid photocatalyst. Interestingly, TiO_2/MgAl-LDO exhibits a higher performance for the photocatalytic reduction of CO_2 into CH_4 under ambient temperature, which might be attributed to the enhanced the adsorption/activation of CO_2 and the adsorption/dissociation of H_2O at the interface of TiO_2 and MgAl-LDO. Comparing with the previous MgAl-LDO/TiO_2, the present work also provides a feasible in situ growth followed by a high temperature calcination process to achieve highly efficient photocatalysts, as well as a depth understanding on the photocatalytic reduction of CO_2 with H_2O over TiO_2.

2 Experimental Section

2.1 Preparation of TiO_2/MgAl-LDO Samples

TiO_2/MgAl-LDO were fabricated via an in situ growth of MgAl-LDH on TiO_2 nanorods followed by a high temperature calcination as Fig. 1. Typically, TiO_2 nanorods were first prepared by using a hydrothermal method. 6 mL HCl was dropped into 15 mL titanium isopropoxide in a 100 mL

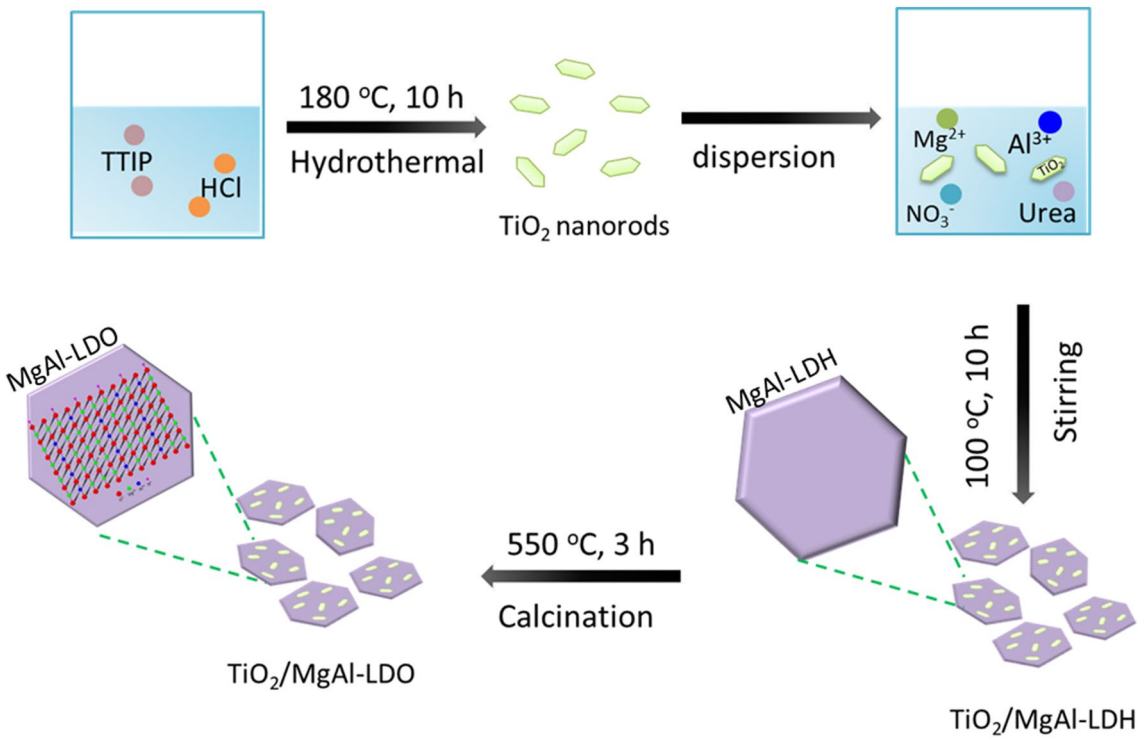

Fig. 1 Schematic illustration of the synthesis process of TiO_2/MgAl-LDO composite

Teflon-lined autoclave at room temperature, and then the mixture was sealed and kept at 180 °C for 36 h. The resulting white precipitates were filtered out and washed with diluent NaOH solution followed by water until the filtrate became neutral. The products (TiO_2) were finally dried overnight in vacuum at 80 °C. Secondly, the desired amount of as-prepared TiO_2 nanorods were dispersed into a 200 mL solution containing 2.10 mmol L^{-1} $Mg(NO_3)_2$, 1.05 mmol L^{-1} $Al(NO_3)_3$ and 0.25 mol L^{-1} urea, followed by the mixture was continuously stirred at 100 °C for 12 h to prepare TiO_2/MgAl-LDH. The obtained TiO_2/MgAl-LDH was finally calcined at 550 °C for 3 h to prepare TiO_2/MgAl-LDO. According to the dosages of TiO_2 with 0.1, 0.05, 0.02 and 0.01 g, TiO_2/MgAl-LDH and TiO_2/MgAl-LDO were correspondingly denoted as TiO_2/MgAl-LDH-*n* and TiO_2/MgAl-LDO-*n* (*n* = 1, 2, 3 and 4).

2.2 Deposition of Pt Cocatalyst

Before the use of photocatalysts, 1 wt% Pt were loaded as cocatalysts by an in situ photodeposition method, using $H_2PtCl_6{\cdot}6H_2O$ as precursors. Taking bare TiO_2 as an example, the deposition of Pt was carried out as following procedure. In typical, 0.1 g TiO_2 was suspended in 25 mL 0.01 mol L^{-1} methanol/H_2O solution containing 1 mg Pt with H_2PtCl_6 (1 mL 1 mg/mL Pt) as precursor. Methanol here was used as hole scavenger. The suspension was irradiated with a 300 W Xe lamp for 1 h, and then the photocatalysts were recovered by filtration, washing with water and dry at 80 °C overnight.

2.3 Characterizations

The crystalline phases were characterized by X-ray powder diffraction (XRD) on a Bruker *D*8 Advance powder diffractometer using Cu *K*a radiation (operating voltage: 40 kV, operating current: 20 mA, scan rate: 5 °/min). Fourier transformed infrared spectroscopy (FT-IR) were recorded on a Bruker VERTEX 70 spectrometer in 4000–400 cm^{-1} using pressed KBr pellet method. UV–visible diffuse reflectance spectra (UV–vis DRS) were recorded on a UV–vis 2600 spectrophotometer (SHIMADZA) and calibrated with Kubelka–Munk method. The morphology was examined by a JSM-7610F scanning electron microscopy (SEM) at an accelerating voltage of 15 kV. Elemental analysis was collected by energy dispersive spectroscopy (EDS, OXFORD X-act) on the SEM (accelerating voltage: 20 kV, probe current: 0.02 mA, Time: 300 s). Transmission electron microscopy (TEM) and high resolution TEM (HRTEM) were performed on a JEOL JEM-2010 TEM (Japan) with the accelerating voltage of 200 kV. The chemical states were characterized on a VG ESCALab 220i XL X-ray photoelectron spectroscopy (XPS) and the binding energies

were calibrated with respect to C1 s (284.8 eV). PEC measurements were performed on a CHI 760D electrochemical workstation (Shanghai) with a three-electrode configuration using $Hg/HgCl_2$ (in sat. KCl) as reference electrode, Pt wire as counter electrode and the prepared films with an active area ca. 0.15 cm^2 as working electrodes. The light source was a 300 W Xe lamp (LS-SXE300CUV, Perfectlight Technology Co. Ltd., Beijing). The electrolyte was 0.5 mol L^{-1} Na_2SO_4 solution. For preparation of working electrodes, the catalysts were dispersed in ethanol to form a homogeneous slurry, and then the slurry was directly casted on an F-doped SnO_2-coated glass (FTO, 1 cm × 2 cm). The film was dried at 353 K for 1 h and then thermally treated at 573 K for 2 h. The transient photocurrent was also conducted at the potential of 0.23 V (vs. SCE).

CO_2 and NH_3 temperature-programmed desorption (CO_2-TPD and NH_3-TPD) experiments were carried out using a Micromeritics AutoChem II 2920 Automated Catalyst Characterization System. Typically, 0.12 g of sample was placed in a quartz reactor for each test. Before introducing CO_2 or NH_3 by impulse injections, the sample was pretreated in a He flow (50 mL min^{-1}) at 300 °C for 2 h and then cooled down to 50 °C in He flow. After saturation adsorption of CO_2 or NH_3, the sample was heated in He from 50 to 550 °C at a heating rate of 10 °C min^{-1} and the TPD profile was recorded with a thermal conductivity detector. The areas under the TPD peaks with the normalized base line were integrated to determine the amount of desorbed CO_2 or NH_3 during TPD.

2.4 Photocatalytic Reduction of CO_2 with H_2O

The photocatalytic reduction of CO_2 with H_2O was carried out using gas–solid mode in a Pyrex reaction cell connected to a closed gas circulation and evacuation system. The light source was a top irradiated 300 W Xe lamp (LS-SXE300 CUV, Beijing Perfectlight Technology Co. Ltd). Typically, 20 mg of catalyst was evenly dispersed onto a glass-sheet (1.5 cm × 2 cm), and then was placed on the holder in the upper region of the reactor, in which 40 mL water was charged on the bottom in advance. The reactor was sealed and degassed for 30 min, and then CO_2 was bubbled slowly till the pressure up to 1 atm. Finally, the reaction was conducted under light irradiation at 20 °C. The generated CO and CH_4, as well as H_2 and O_2, were determined by an on-line GC 7900 gas chromatograph (Shanghai Tianmei) equipped with methanator, flame ionization detector (FID) and thermal conductivity detector (TCD), and the relative standard deviations for the amounts of H_2, CO and CH_4 formed were < 5%.

2.5 Calculation of Apparent Quantum efficiency (AQE)

The experimental results indicated CH_4 and CO were the main reduction products for CO_2, thus AQE was defined as the total extracted electron in CH_4 and CO divided by the number of incident photons (Eq. 1).

$$AQE = \frac{8 \times N_{CH4} + 2 \times N_{CO}}{N_I} \times 100\%, \quad (1)$$

where N_{CH4}, N_{CO} and N_I represent the numbers of evolved CH_4, evolved CO and incident photons. 8 and 2 are the numbers of the required electrons for the conversion of CO_2 to CH_4 and CO. The experiment was performed with Xe lamp equipped with band-pass filters of 310, 330, 350 and 370 nm, respectively.

3 Results and Discussion

3.1 XRD Anallysis

Figure 2a exhibits XRD patterns of TiO_2 and TiO_2/MgAl-LDH. The reflections in TiO_2 matches well with that of rutile TiO_2 [31]. All TiO_2/MgAl-LDH show additional peaks at $2\theta = 11.8^o$, 23.6^o, 35.9^o and 47.2^o, corresponding to (003) (006), (012) and (018) planes of hexagonal MgAl-LDH [32]. In addition, with the decrease of TiO_2 content, the diffraction peaks of MgAl-LDH intensify gradually at the expense of TiO_2 peaks, reflecting their respective contents in the TiO_2/MgAl-LDH composites. After being calcined, all the calcined TiO_2/MgAl-LDH composites show a high crystallinity of TiO_2 rutile phase with complete disappearance of the LDH-related reflections (Fig. 2b). The absence of typical reflection peaks of MgAl-LDO suggested that calcination at 550 °C destroyed the crystal structure of LDH. No other new peaks related to mixed oxides of magnesium and aluminum appeared, indicating that LDH was transformed to a nearly amorphous LDO phase during the calcination process.

3.2 FT-IR and UV–Vis DRS Analysis

FT-IR spectra confirmed the difference of bonding types about TiO_2/MgAl-LDH and TiO_2/MgAl-LDO. As shown in Fig. 3a, the broad band at 3432 cm^{-1} was corresponded to the stretching mode of −OH (ν(OH)) of the interlayer H_2O molecules and hydroxyl groups in the brucite-like layers and the weak peak at 1640 cm^{-1} was attributed to the bending vibration of (H–O–H) of interlayer H_2O molecules in TiO_2/MgAl-LDH, which these band become less intense when TiO_2/MgAl-LDH nanocomposite was calcined to

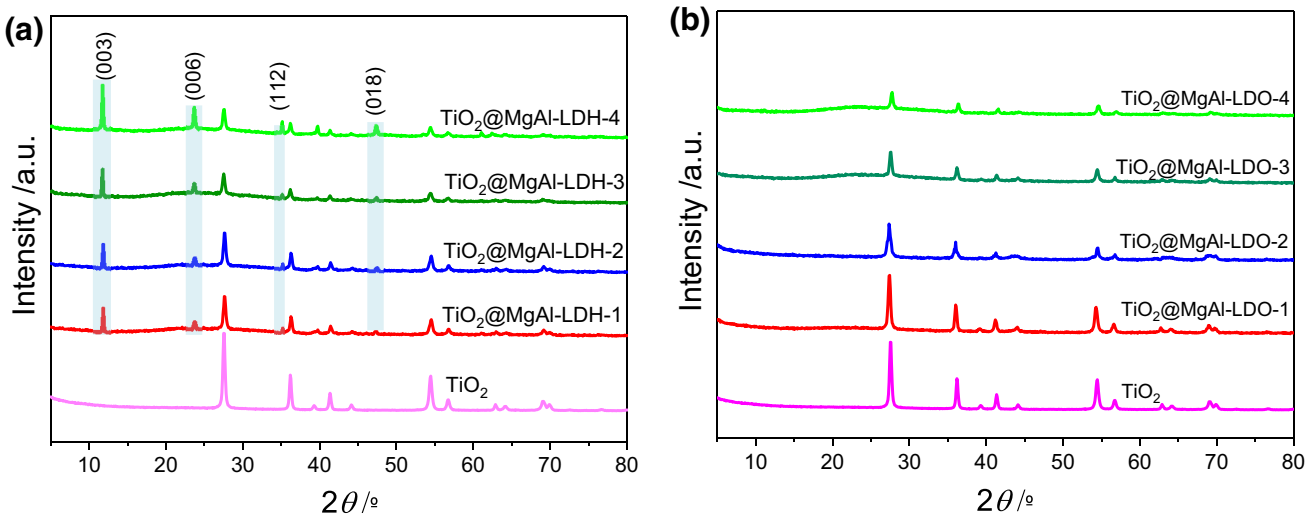

Fig. 2 XRD patterns of the synthesized **a** TiO_2/MgAl-LDH-n and **b** TiO_2/MgAl-LDO-n

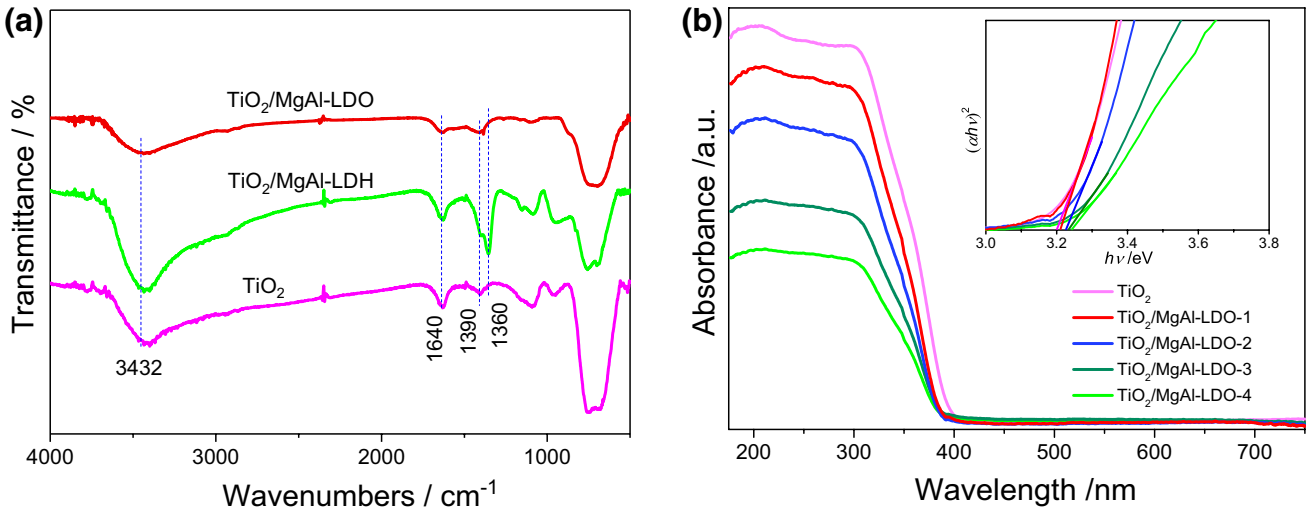

Fig. 3 **a** FT-IR spectra of TiO_2, TiO_2/MgAl-LDH-2 and TiO_2/MgAl-LDO-2; **b** UV–vis DRS of TiO_2 and TiO_2/MgAl-LDO-n. The inset shows slight changes on the bandgap between TiO_2 and TiO_2/MgAl LDO-n

TiO_2/MgAl-LDH. The characteristic vibration at 1360 and 1380 cm^{-1} associated with the interlayer anions (CO_3^{2-} and NO_3^-) in the FTIR spectra of TiO_2/MgAl-LDH become very weak in TiO_2/MgAl-LDO nanocomposite [33–36]. These results indicated that the interlayer anions of LDH were destroyed via dehydration, dehydroxylation, decarbonation and denitration, leading to the formation of LDO during the calcination process. The bands in the range of 500–800 cm^{-1} were attributed to the lattice vibrations of M–O lattice and M–O–M (M = Mg, Al and Ti) [37, 38] and the similar peaks were also observed in the FT-IR spectrum of TiO_2/MgAl-LDH, indicating that the basic bonding types of TiO_2/MgAl-LDO is maintained after calcination treatment. UV–vis DRS (Fig. 3b) displays the absorption onset of TiO_2 extends to approximately 390 nm, corresponding to the band gap of 3.2 eV. While all TiO_2/MgAl-LDO exhibit slightly negative shift, that is slight enlarged bandgap, indicating MgAl-LDO causes negligible effects on the optical property of TiO_2. In addition, the absorption intensity of TiO_2/MgAl-LDO samples was decreased with the increase of MgAl-LDO contents, which might be attributed to the decrease of TiO_2 content in the samples.

3.3 SEM and TEM Analysis

The morphologies of as-obtained TiO_2/MgAl-LDH and TiO_2/MgAl-LDO heterostructures were characterized by SEM (Figure S1). As shown, TiO_2 nanorods were randomly

grafted on the surface of MgAl-LDH hexagonal nanoplatelets in the coprecipitation process. Interestingly, after calcination treatment, the morphology TiO_2/MgAl-LDO was similar to those of TiO_2/MgAl-LDH precursor, where the morphologies of MgAl-LDH hexagonal platelets and TiO_2 nanorods were integrally preserved. As shown in Fig. 4a–h, the MgAl-LDO consists of relatively uniform hexagonal platelets with a lateral size in the range of 4–5 μm and a thickness of ca. 160 nm. Moreover, with the decrease of TiO_2 content, the densities of TiO_2 on MgAl-LDO hexagonal platelets were decreased. The SEM image combined with the EDX elemental mappings of representative TiO_2/MgAl-LDO-2 (Figure S2) showed the distribution of four elements (Mg, Al, Ti and O) within the heterostructures, which reveal that TiO_2 supported on MgAl-LDO platelets. The morphology and structural information of the TiO_2/MgAl-LDO loaded with Pt nanoparticles were further revealed by TEM. TiO_2/MgAl-LDO heterostructures display that numerous TiO_2 nanorods are well assembled on MgAl-LDO platelets, confirming the coexistence of TiO_2 and LDO (Fig. 4i–k). The HRTEM image of shows that the lattice spacing of 0.320 nm corresponds to (110) plane of rutile TiO_2 and no obvious lattice fringe is ascribed to MgAl-LDO, indicating LDO might exist in amorphous phase [30]. Besides that, TEM images also exhibit Pt nanoparticles with a diameter of ca. 4 nm are in intimate contact with TiO_2. These results clearly demonstrated that both Pt and LDO are indeed intimately contacted with TiO_2, rather than existing as separate aggregates in the Pt/TiO_2/MgAl-LDO heterostructures.

3.4 XPS Analysis

To unravel the interaction between TiO_2 and MgAl-LDO, the chemical states of TiO_2/MgAl-LDO were examined by XPS. The survey spectrum indicates all expected elements, such as Ti, O, Mg and Al, exist in TiO_2/MgAl-LDO (Figure S3). High resolution XPS (Fig. 5a) reveals Ti 2p3/2 and Ti 2p1/2 located at ~ 458.5 and 464.3 eV in TiO_2 are negatively shifted to ~ 458.1 and 463.8 eV in TiO_2/MgAl-LDO, suggesting a strong electron interaction between TiO_2 and MgAl-LDO. Such interaction will be favorable for the charge separation during the photocatalytic process. To further confirm the enhanced charge separation, the transient photocurrents based on TiO_2 and TiO_2/MgAl-LDO-2 were

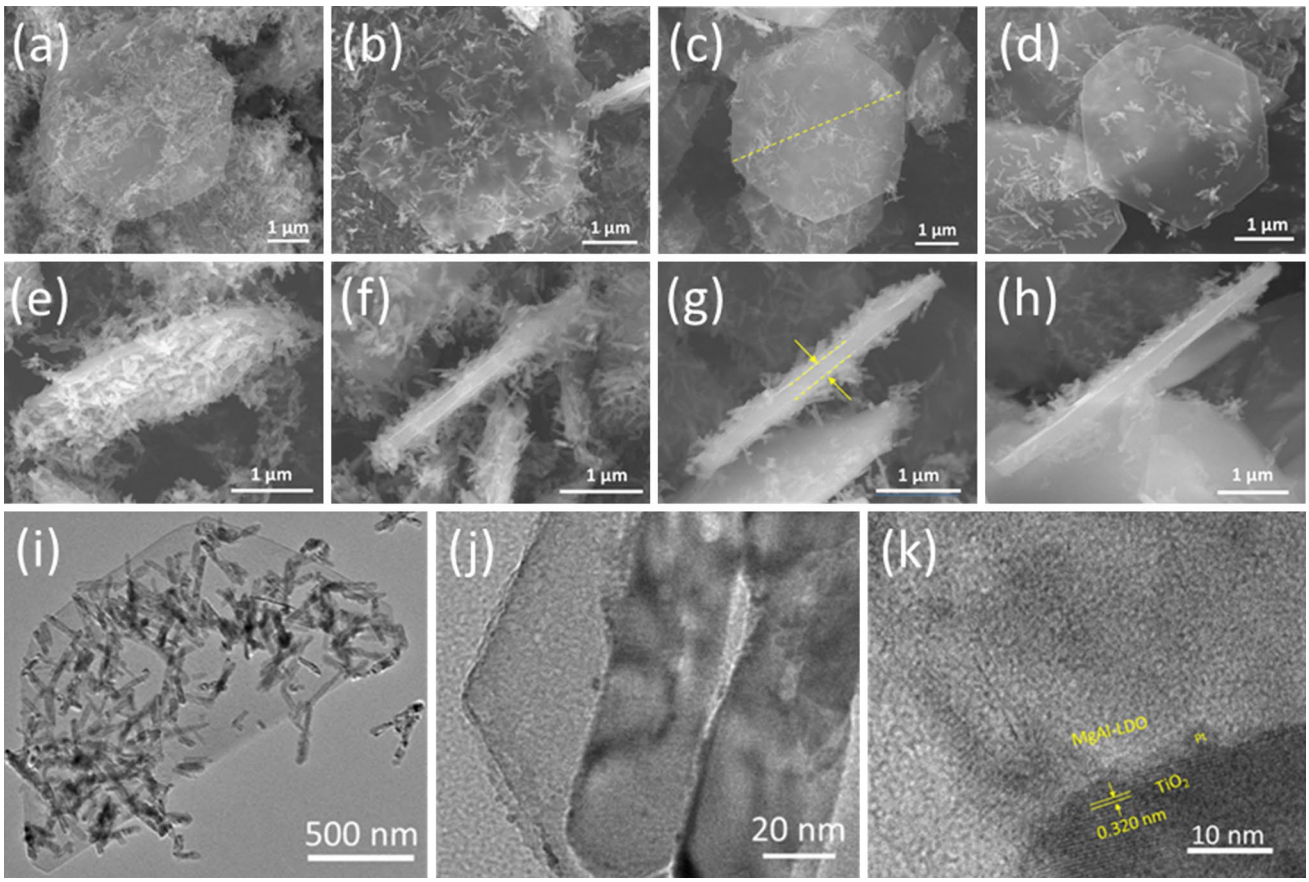

Fig. 4 SEM images of **a** and **e** TiO_2/MgAl-LDO-1, **b** and **f** TiO_2/MgAl-LDO-2, **c** and **g** TiO_2/MgAl-LDO-3, **d** and **h** TiO_2/MgAl-LDO-4. TEM and HRTEM images **i–k** of Pt/TiO_2/MgAl-LDO-2 photocatalyst

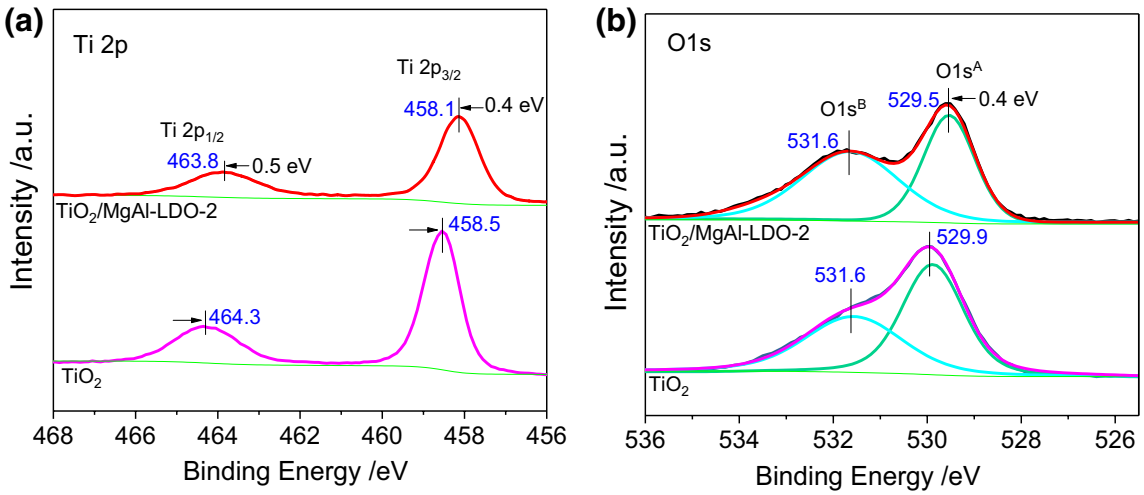

Fig. 5 XPS of **a** Ti 2p and **b** O 1s spectra of TiO_2/MgAl-LDO-2

comparably shown in Figure S4. As seen, comparing with that of TiO_2, the photocurrent density of TiO_2/MgAl-LDO-2 was significantly enhanced, indicating much more effective separation of photogenerated charges over TiO_2/MgAl-LDO-2. Figure 5b displays O 1s spectra for TiO_2 and TiO_2/MgAl-LDO. As shown, the O 1s spectrum of TiO_2 could be well deconvoluted into two peaks at 529.9 eV ($O1s^A$) and 531.6 eV ($O1s^B$) [39], which could be ascribed to the lattice oxygen and the oxygen defects/surface oxygen species with low coordination respectively. After being loaded on MgAl-LDO, the binding energy of $O1s^B$ shows negligible change, while that of $O1s^A$ shows a slight negative shift to 529.5 eV. Such negative shift might be ascribed to the lattice oxygen existed in MgAl-LDO. Due to the lower electronegativity of Mg compared with Ti, the electron cloud density of oxygen was increased. The lattice oxygen with higher electron cloud density would act as much more effective basic sites for the adsorption of CO_2. It is also noted, the intensity ratio of $O1s^B/O1s^A$ increases from 0.48 to 0.63 after TiO_2 being loaded on MgAl-LDO, suggesting an increase of the oxygen defects/surface oxygen species on TiO_2/MgAl-LDO. Such oxygen defects/surface oxygen species would also be favorable to the adsorption and activation of CO_2. In a word, MgAl-LDO load has great potential to facilitate the charge separation and the CO_2 adsorption/activation, thus promotes the photocatalytic reduction of CO_2 over TiO_2.

3.5 Photocatalytic CO_2 Reduction Performance

The photocatalytic activities of TiO_2/MgAl-LDO photocatalysts, including individual TiO_2 and MgAl-LDO with Pt as cocatalyst were evaluated under illumination and the results are shown in Fig. 6. CO and CH_4 were found to be the main and direct products of CO_2 reduction reaction and no other carbonaceous products were observed. The controlled experiments in the absence of light irradiation or catalysts were conducted, and no products could be detected, demonstrating that light irradiation and photocatalysts were essential for photocatalytic reduction of CO_2 with H_2O. On the other hand, neither CO or CH_4 was detected by introducing Ar instead of CO_2, indicating CO or CH_4 were originated from the reduction of CO_2 rather than the residual carbon species in photocatalysts. Figure 6a, b illustrate the evolutions of CO and CH_4 as a function of reaction time over all as-prepared photocatalysts. As shown, the amounts of CO and CH_4 increase almost linearly with reaction time, is indicative of excellent stability of photocatalysts. It is also noticeable that all TiO_2/MgAl-LDO exhibit superior activities of CO and CH_4 evolutions to that of TiO_2. In 8 h of reaction time, CO and CH_4 evolutions over TiO_2 show the minimum yields of 0.14 and 0.033 μmol respectively, while that over TiO_2/MgAl-LDO-2 present the maximum yields of 0.65 and 1.6 μmol respectively. The activities over Pt/TiO_2/MgAl-LDO-2 were obviously enhanced by ca. 4.6- and 48-times respect to that obtained on Pt/TiO_2, indicating MgAl-LDO-2 played vital roles on the photocatalytic reduction of CO_2 over TiO_2. The average rates of CO and CH_4 evolution over TiO_2/MgAl-LDO also exhibit a volcano-type activity against the MgAl-LDO content. This would be due to that excessive amount of MgAl-LDO reduces the content of TiO_2 responded for light absorption, and finally decreases the densities of photogenerated electrons and holes.

The average rates of CO and CH_4 evolution (Fig. 6c) show a clear inversion of CH_4/CO between TiO_2 and TiO_2/MgAl-LDO-n, suggesting MgAl-LDO is beneficial to the selective photocatalytic reduction of CO_2 with H_2O to CH_4 rather than CO. The high selectivity of CH_4 over TiO_2/MgAl-LDO might be resulted from the basic sites provided

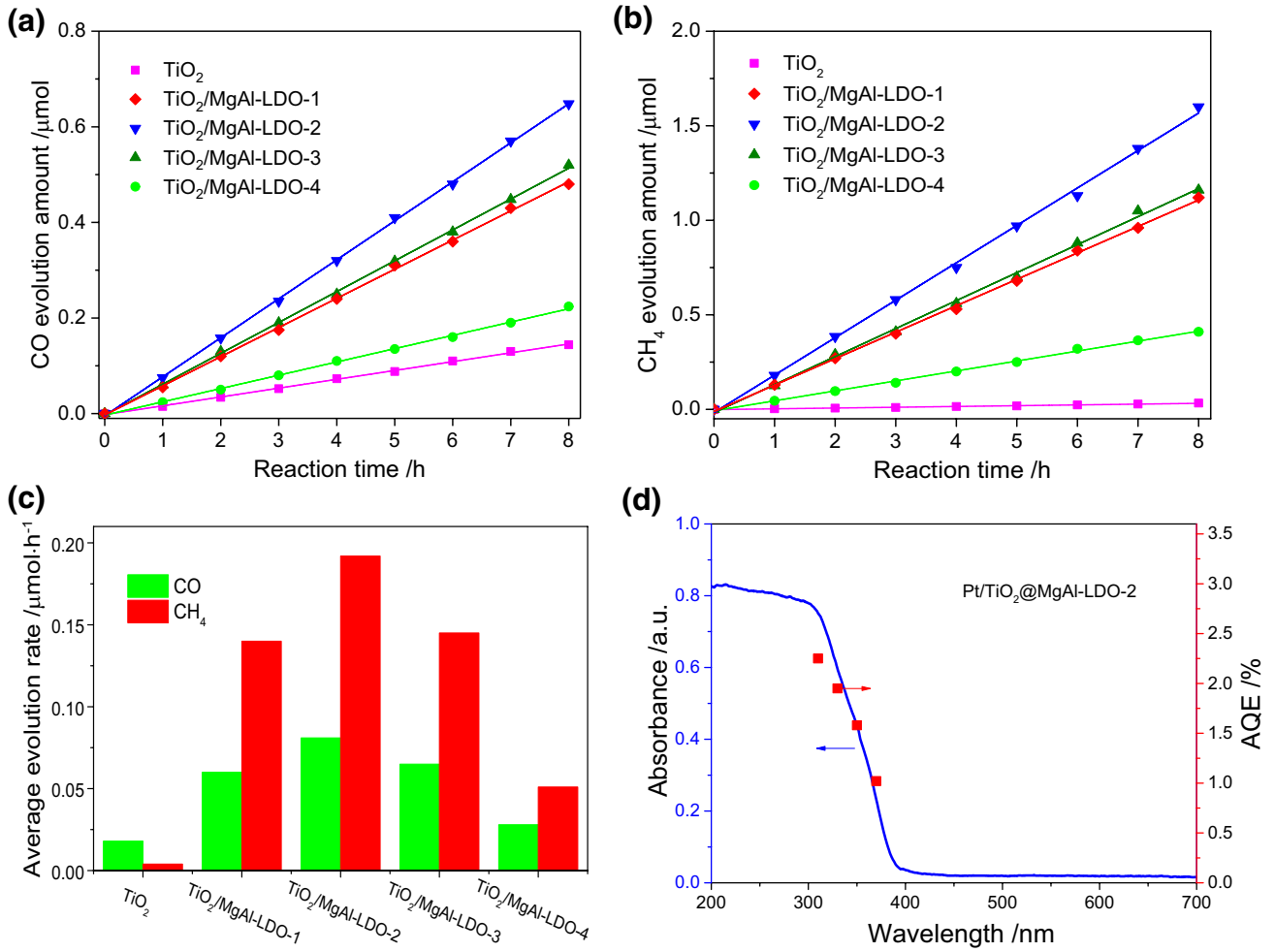

Fig. 6 Time-dependent **a** CO, **b** CH_4 amounts and **c** the average evolution rate of CO and CH_4 over CO over TiO_2 and TiO_2/MgAl-LDO-n photocatalysts. (Conditions: photocatalyst, 0.02 g; cocatalyst, 1 wt% Pt; CO_2 pressure: 1 atm; light source, 300 W xenon lamp; reaction temperature, 20 °C). **d** An AQY on account of CO and CH_4 production by Pt/TiO_2/MgAl-LDO-2 photocatalyst along with the UV–vis DRS spectrum of TiO_2/MgAl-LDO-2

by MgAl-LDO, which is favorable for the preferential stabilization of CO_2 into chemisorbed species and the hydrogenation of CO_2. Comparing with MgAl-LDO/TiO_2 photocatalyst [30], in which MgAl-LDO was used as a modifier of TiO_2, the average rates of CO and CH_4 evolution over TiO_2/MgAl-LDO-2 are about 1.7 and 3.2 times higher than these over MgAl-LDO/TiO_2, respectively. In addition, the amount of O_2 generated form the photocatalytic reduction of CO_2 over Pt/TiO_2/MgAl-LDO-2 was also quantified (Figure S5). The molar ratio of $\left(n_{CO}+4n_{CH_4}\right)/n_{O_2}$ was calculated to be 1.91, which was slightly lower than the theoretical value of 2. The deviation might be attributed to the minor undetectable H_2 or the incomplete vacuum degassing. No matter what, it suggests CO and CH_4 are the main reduction products from the photocatalytic reduction of CO_2. As further investigation, apparent quantum efficiency (AQE), related to the light energy-chemical energy conversion over TiO_2/MgAl-LDO-2, was also calculated. As seen in Fig. 6d, AQE is highly dependent on the incident wavelength, where AQE decreases with the increase of incident wavelength in 300–400 nm of the optical absorption spectrum of TiO_2/MgAl-LDO-2. AQE for TiO_2/MgAl-LDO-2 at 350 nm is shown as ca. 1.58%, which is ca. 22 times higher than that of TiO_2 (0.07%). While AQEs for TiO_2/MgAl-LDO-1, TiO_2/MgAl-LDO-3 and TiO_2/MgAl-LDO-4 at 350 nm are 1.20%, 1.22% and 0.38%, respectively. It is further confirmed that the introduce of MgAl-LDO platelets into Pt/TiO_2 photocatalyst is beneficial to improve the utilization efficiency of solar irradiation. Finally, the stability for the photocatalysts was examined by using Pt/TiO_2/MgAl-LDO-2. Before the cycle, the system was degassed with vacuum and then bubbled with CO_2 to atmospheric pressure. As shown in Figure S6, similar activities, without significant decrease of the amounts for CO and CH_4 formation, are observed in the

second runs, suggesting the prepared photocatalyst possesses excellent stability.

3.6 CO_2- and NH_3- TPD Characterization

Apparently, MgAl-LDO has greatly promote the photocatalytic reduction of CO_2 over TiO_2; that is, CO and CH_4 evolution, the selectivity of CH_4 and AQE have been boosted after TiO_2 being loaded on MgAl-LDO. To understand the mechanism that MgAl-LDO enhanced CO_2 reduction over TiO_2, CO_2- and NH_3- temperature-programmed desorption (CO_2-TPD and NH_3-TPD) were carried out based on the as-prepared samples (Fig. 7). As shown in Fig. 7a, CO_2-TPD for TiO_2/MgAl-LDO exhibit similar profiles. The profiles could be well deconvoluted into four desorption peaks at low temperature (140 °C), moderate temperature (210 and 280 °C) and high temperature (380 °C), corresponding to the bicarbonate binding on surface OH, bidentate carbonate of chemisorbed CO_2 on Mg^{2+}-O^{2-} pairs and monodentate carbonate associated with low-coordination O^{2-} anions [40–42]. The intensities CO_2-TPD for TiO_2/MgAl-LDO are also observed to be increased with the increase content of MgAl-LDO, suggesting MgAl-LDO plays a crucial role that enhance CO_2 adsorption. By taking the acidic character of CO_2, MgAl-LDO obviously possesses much more and stronger basic sites than that in TiO_2 for CO_2 adsorption [32, 43]. The absorbed CO_2 interacted with such basic sites and were activated by forming bicarbonate, bidentate carbonate and monodentate carbonate. It then deduced MgAl-LDO could promote the photocatalytic reduction of CO_2 over TiO_2 by improving the adsorption and activation of CO_2 molecule, thus facilitating the reduction half-reaction of CO_2 with H_2O.

The acidic properties of these samples were probed by TPD of NH_3 preadsorbed at room temperature. NH_3-TPD for TiO_2 in Fig. 7b shows a weak desorption peak at 130–280 °C, indicating a little amount of acidity sites on TiO_2 surface. According to literature, the acidic sites on the catalyst are defined in three types according to the different temperature range of NH_3 desorption: i.e. weak acidic sites at 150–250 °C; intermediate acidic sites at 250–450 °C and strong acidic sites at 450–540 °C [44, 45]. As for TiO_2/MgAl-LDO-n samples, four desorption peaks at around 130, 225, 375 and 450 °C were obtained by fitting NH_3-TPD plots, meaning that the weak, intermediate and strong acidic sites coexist in TiO_2/MgAl-LDO. While only the weak and intermediate exist in TiO_2. Moreover, the intensities for NH_3 desorption peaks gradually increase with the increase of MgAl-LDO content in TiO_2/MgAl-LDO. In agreement with literatures, the peaks at 130, 225 and 375 °C could be Lewis acid sites, while the peak at 450 °C could identified to Brønsted acid sites. Lewis acid sites in TiO_2/MgAl-LDO are located on the cations of Al-O-Mg species in MgAl-LDO due to the substitution of Mg^{2+} by Al^{3+} MgO lattice, while Brønsted acid sites are derived from surface OH groups [32, 46]. It should be noted that the peak related to Brønsted acid sites is quietly weak compared with the peaks associated with Lewis acid sites, indicating that Lewis acidity is the predominant acidity in TiO_2/MgAl-LDO. Such acidic sites could act as active sites for water adsorption and activation, due to the feasible coordination of H_2O to Lewis acidic sites, thus promoting the H_2O oxidation half-reaction.

3.7 Possible Mechanism

Based upon above discussion, it could conclude MgAl-LDO plays a curial role that supplies abundant acidic and basic sites for the adsorption/activation of H_2O and CO_2, subsequently facilitates the half-reactions of H_2O oxidation and CO_2 reduction [47, 48]. A possible mechanism

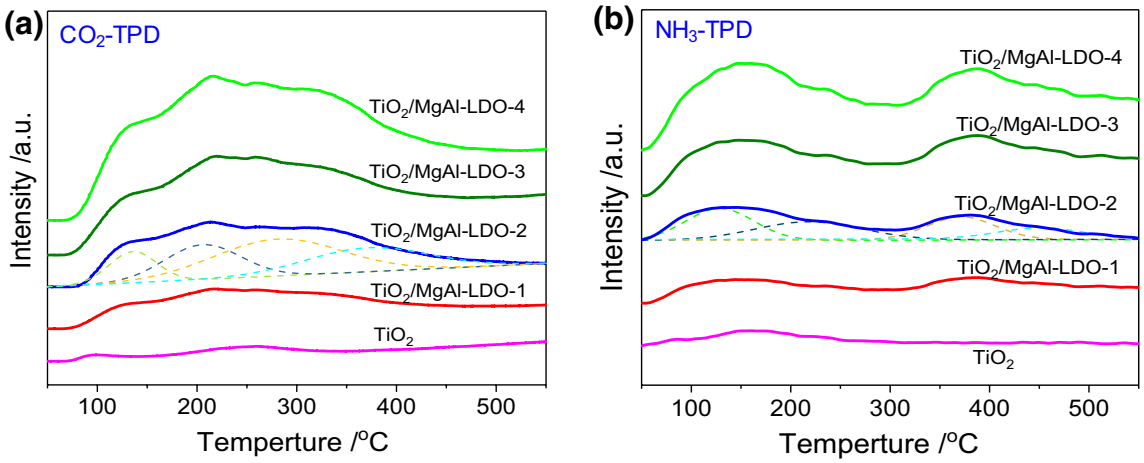

Fig. 7 **a** CO_2-TPD and **b** NH_3-TPD profiles of TiO_2/MgAl-LDO samples

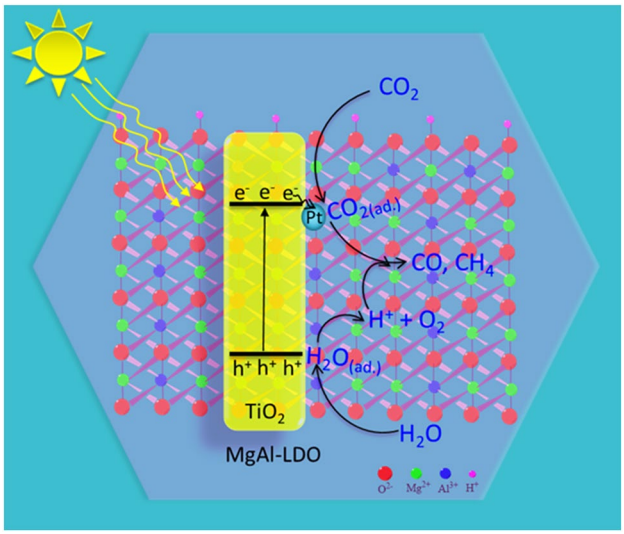

Fig. 8 Schematic illustration of the proposed mechanism for photocatalytic reduction of CO_2 with H_2O over TiO_2/MgAl-LDO photocatalyst

for the photocatalytic reduction of CO_2 with H_2O over Pt/TiO_2/MgAl-LDO was schematically illustrated in Fig. 8. In this photocatalytic reaction system, rutile TiO_2 nanorods are the fountain of photogenerated electron–hole (e^-–h^+) pairs, while the loaded Pt played a key role to gather photogenerated electrons (e^-) from the conduction band of rutile TiO_2 nanorods and serve as reduction active sites. CO_2 and H_2O were first absorbed and activated to form $CO_{2(ad.)}$ and $H_2O_{(ad.)}$ at the basic and acidic sites of TiO_2/MgAl-LDO respectively. Under light irradiation, the electrons (e^-) in valence band (VB) of TiO_2 were excited and transferred to conductive band (CB), and then migrated to Pt, nearby which $CO_{2(ad.)}$ accepted e^- to proceed the reduction half-reaction. On the other hand, the holes (h^+) left on the surface of TiO_2 reacted with the near $H_2O_{(ad.)}$ to complete the water oxidation half-reaction. By assistance of the protons from H_2O dissociation, $CO_{2(ad.)}$ were reduced into CO and CH_4 [49–51]. Meanwhile, $H_2O_{(ad.)}$ were oxidized to O_2.

4 Conclusion

In summary, TiO_2/MgAl-LDO photocatalysts were successfully fabricated and exhibited enhanced photocatalytic CO_2 reduction performance with H_2O. The enhanced performance was benefited from the abundant acidic and basic sites supplied by MgAl-LDO. The optimal TiO_2/MgAl-LDO showed the CO and CH_4 yields of 0.65 and 1.6 μmol in 8 h reaction, which were ca. 4.6 and 48 times with respect to that for TiO_2. The work indicates the same importance of acidic and basic sites for photocatalytic CO_2 reduction with H_2O. It is expected modifiers or supporters with abundant acidic and basic sites will be beneficial to the photocatalytic CO_2 reduction with H_2O over various semiconductors. It will also stimulate us to explore much more efficient photocatalysts for CO_2 reduction with H_2O.

Acknowledgements The work was supported by the National Natural Science Foundation of China (51502078), the Major Project of Science and Technology, Education Department of Henan Province (17B610003, 19A150018 and 19A150019), Henan University (YQPY20170013), the program for Science & Technology Innovation Team in Universities of Henan Province (19IRTSTHN029).

References

1. Xiong J, Song P, Di J, Li H (2019) Appl Catal B 256:117788
2. Munawar K, Jarnuzi G, Tribidasari AI, Aminah U (2019) Renew Sustain Energy Rev 113:109246
3. Liu LJ, Jiang YQ, Zhao HL, Chen JT, Cheng JL, Yang K, Li Y (2016) ACS Catal 6:1097
4. Wang CL, Sun ZX, Zheng Y, Hu YH (2019) J Mater Chem A 7:865
5. Voiry D, Shin HS, Loh KP, Chhowalla M (2018) Nat Rev Chem 2:0105
6. Inoue T, Konishi S, Fujishima A, Honda K (1979) Nature 277:637
7. Shehzad N, Tahir M, Johari K, Murugesan T, Hussain M (2018) J CO2 Util 26:98
8. Zhang T, Low J, Koh K, Yu J, Asefa T (2018) ACS Sustain Chem Eng 6:531
9. Zhang L, Xie C, Jiu H, Meng Y, Zhang Q, Gao Y (2018) Catal Lett 148:2812
10. Li XB, Xiong J, Gao XM, Huang JT, Feng ZJ, Chen Z, Zhu YF (2019) J Alloy Compd 802:196
11. Yang Y, Wu JJ, Xiao TT, Tang Z, Shen JY, Li HJ, Zhou Y, Zou ZG (2019) Appl Catal B 255:117771
12. Zhang X, Zhang X, Wang X, Wang D, Liu L, Ye J (2018) Chin J Catal 39:973
13. Xu Q, Yu J, Zhang J, Zhang J, Liu G (2015) Chem Commun 51:7950
14. Zhao H, Liu L, Andino JM, Li Y (2013) J Mater Chem A 1:8209
15. Wang W, An W, Ramalingam B, Mukherjee S, Niedzwiedzki DM, Gangopadhyay S, Biswas P (2012) J Am Chem Soc 134:11276
16. Tseng IH, Wu J, Chou HY (2004) J Catal 221:432
17. Wei Y, Wu X, Zhao Y, Wang L, Zhao Z, Huang X, Liu J, Li J (2018) Appl Catal B 236:445
18. Abdullah H, Khan MMR, Ong HR, Yaakob Z (2017) J CO2 Util 22:15
19. Ran J, Jaroniec M, Qiao SZ (2018) Adv Mater 30:1704649
20. Tu W, Zhou Y, Zou Z (2014) Adv Mater 26:4607
21. Nolan M (2018) J Mater Chem A 6:9451
22. Ma Y, Wang Z, Wang J, Xu X (2017) Chin J Catal 38:1956
23. He Z, Tang J, Shen J, Chen J, Song S (2016) Appl Surf Sci 364:416
24. Liu L, Zhao C, Zhao H, Pitts D, Li Y (2013) Chem Commun 49:3664
25. Feng X, Pan F, Zhao H, Deng W, Zhang P, Zhou H, Li Y (2018) Appl Catal B 238:274
26. Li H, Wu X, Wang J, Gao Y, Li L, Shih K (2016) Int J Hydrog Energ 41:8479
27. Li Q, Zong L, Li C, Yang J (2014) Appl Surf Sci 319:16
28. Wang F, Zhou Y, Li P, Kuai L, Zou Z (2016) Chin J Catal 37:863
29. Liu Q, Han Y, Cai J, Crumlin EJ, Li Y, Liu Z (2018) Catal Lett 148:1686

30. Chong R, Su C, Du Y, Fan Y, Ling Z, Chang Z, Li D (2018) J Catal 363:92
31. Delidovich I, Palkovits R (2015) J Catal 327:1
32. Gao Y, Zhang Z, Wu J, Yi X, Zheng A, Umar A, O'Hare D, Wang Q (2013) J Mater Chem A 1:12782
33. Zou Y, Wang X, Wu F, Yu S, Hu Y, Song W, Liu Y, Wang H, Hayat T, Wang X (2017) ACS Sustain Chem Eng 5:1173
34. Koilraj P, Kamura Y, Sasaki K (2017) ACS Sustain Chem Eng 5:9053
35. Wang G, Wang B, Su C, Li D, Zhang L, Chong R, Chang Z (2018) J Catal 359:287
36. Flores-Flores M, Luevano-Hipolito E, Torres Martinez LM, Morales-Mendoza G, Gomez R (2018) J Photochem Photobiol A 363:68
37. Chen D, Li Y, Zhang J, Zhou J, Guo Y, Liu H (2012) Chem Eng J 185:120
38. Chang P, Lee T, Chang Y, Chen S (2013) Chemsuschem 6:1076
39. Dou Y, Zhang S, Pan T, Xu S, Zhou A, Pu M, Yan H, Han J, Wei M, Evans DG, Duan X (2015) Adv Funct Mater 25:2243
40. Zhang S, Cai W, Yu J, Ji C, Zhao N (2017) Chem Eng J 310:216
41. McKenzie AL, Fishel CT, Robert DJ (1992) J Catal 138:547
42. Feng J, Ma C, Miedziak PJ, Edwards JK, Brett GL, Li D, Du Y, Morgan DJ, Hutchings GJ (2013) Dalton Trans 42:14498
43. Arbeláez O, Orrego A, Bustamante F, Villa AL (2016) Catal Lett 146:725
44. Chen H, Ruan H, Lu X, Fu J, Langrish T, Lu X (2018) Mol Catal 445:94
45. Li C, Zhou G, Wang L, Dong S, Li J, Cheng T (2011) Appl Catal A 400:104
46. Dixit M, Mishra M, Joshi PA, Shah DO (2013) J Ind Eng Chem 19:458
47. Stolarczyk JK, Bhattacharyya S, Polavarapu L, Feldmann J (2018) ACS Catal 8:3602
48. Zhao G, Huang X, Wang X, Wang X (2017) J Mater Chem A 5:21625
49. Karamian E, Sharifnia S (2016) J CO2 Util 16:194
50. Kočí K, Obalová L, Šolcová O (2010) Chem Process Eng 31:395
51. Tan S, Zou L, Hu E (2008) Catal Today 131:125

Affiliations

Ruifeng Chong[1] · Caihong Su[1] · Zhenzhen Wang[1] · Zhixian Chang[1] · Ling Zhang[1] · Deliang Li[1]

✉ Zhixian Chang
chzx19@henu.edu.cn

✉ Deliang Li
lideliang@henu.edu.cn

[1] Institute of Upconversion Nano-scale Materials, College of Chemistry and Chemical Engineering, Henan University, Kaifeng 475001, China